HHS Public Access

Author manuscript

Nat Mater. Author manuscript; available in PMC 2021 May 09.

Published in final edited form as:

Nat Mater. 2021 April ; 20(4): 560–569. doi:10.1038/s41563-020-00844-w.

Activating an adaptive immune response from a hydrogel scaffold imparts regenerative wound healing.

Donald R. Griffin[1,2,†], **Maani M. Archang**[3,†], **Chen-Hsiang Kuan**[4,5,6], **Westbrook M. Weaver**[3,&], **Jason S. Weinstein**[7], **An Chieh Feng**[8], **Amber Ruccia**[8], **Elias Sideris**[1], **Vasileios Ragkousis**[8], **Jaekyung Koh**[3], **Maksim V. Plikus**[4,5,9,10], **Dino Di Carlo**[3], **Tatiana Segura**[3,6,*], **Philip O. Scumpia**[8,11,*]

[1.]Chemical and Biomolecular Engineering Department, University of California, Los Angeles, Los Angeles, CA

[2.]Biomedical Engineering, Chemical Engineering, University of Virginia, Charlottesville, VA

[3.]Bioengineering Department, University of California, Los Angeles, Los Angeles, CA

[4.]Department of Developmental and Cell Biology, University of California, Irvine, CA

[5.]Sue and Bill Gross Stem Cell Research Center, University of California, Irvine, Irvine, CA

[6.]Division of Plastic Surgery, Department of Surgery, National Taiwan University Hospital, Taipei, Taiwan

[7.]Department of Medicine, Rutgers –New Jersey Medical School, Newark, NJ

[8.]Division of Dermatology, Department of Medicine, David Geffen School of Medicine, University of California, Los Angeles, Los Angeles, CA

[9.]Center for Complex Biological Systems, University of California, Irvine, Irvine, CA

[10.]NSF-Simons Center for Multiscale Cell Fate Research, University of California-Irvine, Irvine, CA

[11.]Department of Dermatology, VA Greater Los Angeles Healthcare System-West Los Angeles, Los Angeles, California

Abstract

[*]To whom correspondence should be addressed: Philip O. Scumpia, PScumpia@mednet.ucla.edu, Tatiana Segura, Tatiana.segura@duke.edu.

[&]Current address Tempo Therapeutics, San Diego, CA 92109

Author Contribution

D.R.G., P.O.S., and T.S. conceived the experiments. D.R.G., W.M.W, E.S., M.M.A., and J.K. carried out microfluidic design and fabrication, and D.D.C. oversaw microfluidic design and fabrication. D.R.G., M.M.A., C.H.K., W.M.W, J.S.W., A.C.F., E.S., A.R., V.R., P.O.S. performed experiments. D.R.G., M.M.A., J.S.W., A.R., M.V.P., T.S. and P.O.S. analyzed and interpreted data. D.R.G., M.M.A., P.O.S., and T.S. wrote the manuscript and all authors discussed the results and contributed to writing portions of the manuscript and editing the manuscript. D.R.G. and M.M.A. contributed equally to this work.

The co-principal investigators are P.O.S. and T.S.

[†]Donald R. Griffin and Maani M. Archang contributed equally to this work.

Competing financial interests

D.R.G., W.M.W., D.D.C., T.S., and P.O.S. have a financial interest in Tempo Therapeutics, which aims to commercialize MAP technology.

Microporous annealed particle (MAP) scaffolds are flowable, in situ crosslinked, microporous scaffolds composed of microgel building blocks and were previously shown to accelerate wound healing. To promote more extensive tissue ingrowth before scaffold degradation, we aimed to slow MAP degradation by switching the chirality of the crosslinking peptides from L- to D-amino acids. Unexpectedly, despite showing the predicted slower enzymatic degradation *in vitro*, D-peptide crosslinked MAP hydrogel (D-MAP) hastened material degradation *in vivo* and imparted significant tissue regeneration to healed cutaneous wounds, including increased tensile strength and hair neogenesis. MAP scaffolds recruit IL-33 type 2 myeloid cells, which is amplified in the presence of D-peptides. Remarkably, D-MAP elicited significant antigen-specific immunity against the D-chiral peptides, and an intact adaptive immune system was required for the hydrogel-induced skin regeneration. These findings demonstrate that the generation of an adaptive immune response from a biomaterial is sufficient to induce cutaneous regenerative healing despite faster scaffold degradation.

The goal of regenerative medicine is to restore tissue function back to physiological activity. For biomaterial scaffolds, the optimal strategy to achieve this requires balancing material degradation with tissue regrowth. Clinical/patient factors contribute to a wide variation in chemical and physical parameters *in situ*, which makes striking a degradative-regenerative balance particularly difficult. Our recent development of a flowable, granular biomaterial, known as MAP (Microporous Annealed Particle) gel, provides a new approach to make the balance more feasible[1]. The MAP gel is composed of randomly packed microsphere building blocks with a continuous network of interconnected micrometer-scale void spaces that allows for the infiltration of surrounding tissue without the prerequisite degradation of material[1,2]. This unique design resulted in improved tissue closure and improved vascularization relative to a nanoporous (but chemical formulation equivalent) hydrogel in a cutaneous wound model[1].

Mechanical support to the growing tissue by scaffolds is inherently impacted by the degradation rate of the scaffold[3]. For MAP scaffolds, degradation leads to a slow loss of porosity and reduced tissue ingrowth prior to dissolution. We hypothesized that slowing the degradation rate of MAP scaffolds would maintain the porosity and influence both wound closure rate and regenerated tissue quality.

Changing the chirality of peptide moieties leads to a diminished degradation rate by endogenously present enzymes[4,5]. The use of chirality was made more attractive by the fact that polypeptides of D-enantiomeric amino acids are do not typically elicit a robust immune response and are considered poorly immunogenic[5]. Previously, we have used amino acid chirality to tune the proteolysis rate of peptide nanocapsules for controlled release of encapsulated growth factors[4]. Therefore, we chose to use an analogous approach to slow the enzymatic degradation of our MAP scaffold by switching the chirality of the peptide crosslinker (e.g. L- to D-chirality at the site of matrix metalloprotease (MMP)-mediated bond cleavage). We hypothesized that this approach would maintain the hydrogel micro-environment (e.g. charge-based interactions and hydrophobicity), while increasing the long-term hydrogel integrity to allow full infiltration of cells, thus providing a greater integration of the entire construct with the host tissue.

In the current study, we investigate how MAP hydrogels cross-linked with either D- or L-amino acid crosslinking peptides affect wound healing and skin regenerative responses using murine wound models. We provide evidence that activation of specific immune responses by the D-amino acid crosslinked MAP hydrogels elicit skin regeneration. While immunity undoubtedly activates the foreign body response and eventual fibrosis of some implanted biomaterials[6,7], the activation of the correct immune responses may enhance the regenerative ability of a biomaterial[8,9].

D-chiral crosslinker peptides slow MAP degradation in vitro.

We first used enantiomeric chemistry to change degradation rate without changing the initial material properties (e.g. hydrophobicity, mesh size, and charge) of the hydrogel[4]. All amino acids at the site of enzymatic cleavage for the MMP-degradable peptide were changed to D-amino acids (Ac-GCRDGPQ$_D$GI$_D$W$_D$GQDRCG-NH2, D-peptide). We matched the stiffness (i.e. storage modulus) by rheology of both the D-peptide MAP (D-MAP) and L-peptide (L-MAP) formulations to that used in our previous MAP-based cutaneous application (~500Pa; Figure 1a). After formulation optimization, we generated the microsphere particles using a previously published microfluidic technique[1]. Following application of Collagenase I to L-MAP, D-MAP or a 50% mixture of D-MAP and L-MAP (1:1 L/D-MAP), the L-MAP hydrogel degraded within minutes, while the degradation of D-MAP by itself or within a mixture with L-MAP was minimal even after an 1 hour (Figure 1b and Supplementary Figure 1).

D-chiral crosslinker peptides enhance MAP degradation in vivo.

We next examined how D-MAP compares to L-MAP *in vivo* in a murine splinted excisional wound model[1,10]. We did not find any difference in wound closure rate, or any increased erythema or gross signs of inflammation in wounds treated with D-MAP, L-MAP, or a 1:1 mixture of L/D MAP any time after treatment (shown Day 3 and Day 6 after wounding, Supplementary Figure 2a). When comparing wound closure to sham treatment (no hydrogel), we found that 1:1 mixture of L/D MAP induced more rapid wound closure (assessed on Day 9 after wounding) than sham (Supplementary Figure 2b), similar to previous results with L-MAP hydrogel[1].

Since no differences in wound closure results were noted, we next examined whether the degradation of hydrogels containing D amino acid cross-linkers was slowed *in vivo* by examining excised tissue 21 days after the wound was completely healed. Unexpectedly, histological sections of wounds treated with D-MAP or a 1:1 L/D-MAP hydrogel mixture displayed minimal to no hydrogel persistence 21 days after wounding, nearing levels seen in mice not treated with hydrogel (Sham), whereas wounds treated with L-MAP hydrogel displayed large amounts of hydrogel remaining (Figure 1c–f).

D-MAP hydrogels impart tissue regenerative properties.

Of note, initial examination of histologic sections of D-MAP and 1:1 L/D-MAP displayed a much different overall appearance than that of healed sham- or L-MAP-treated wounds.

Previous reports suggest that, unlike large excisional wounds in adult mice (wounds larger than 1×1 cm) that result in significant regenerative healing with wound induced hair neogenesis (WIHN)[11–13], wounds smaller than 1×1cm in mice, like the punch biopsies performed in our studies, typically heal without regeneration of new hair and fat and, instead, form scars[12,14,15]. Despite these reports, when the correct regenerative cues are provided from wound fibroblasts, through transgenic activation of specific Hedgehog signals, small wounds can regenerate[16]. Consistent with these results, histological examination of 4-mm excisional splinted wounds in mice that did not receive hydrogel (sham) displayed the typical appearance of scar tissue with a flattened epidermis, a thinned dermis with horizontally-oriented collagen bundles, vertically-oriented blood vessels, and lack of hair follicles and sebaceous glands (Figure 1c, g–i). Tissue from mice treated with L-MAP hydrogel displayed a similar appearance, but with thicker overall tissue compared to sham wounds, due to the substantial residual L-MAP hydrogels (Figure 1d, g). Within the dermis surrounding the hydrogel, fibroblasts secreting collagen/extracellular matrix and blood vessels formed between the hydrogel microparticles (Figure 1d). Only rare hair follicles and associated sebaceous glands were observed in the wound areas (Figure 1d, h–i). Remarkably, examination of histological sections of the D-MAP- or 1:1 L/D-MAP-treated tissue revealed a *de novo* regenerated appearance. The overlying epidermis often displayed physiological undulation, while numerous immature-appearing hair follicles were seen spanning the length of the healed full thickness injury (Figure 1e–i). Samples treated with D-MAP or 1:1 L/D-MAP also displayed increased skin thickness despite less hydrogel remaining in these samples (Figure 1f). Many samples also displayed epidermal cyst formation. In samples that displayed residual hydrogel, hair follicles were apparent directly overlying the degrading MAP hydrogel particles (Supplementary Figure 2c). The presence of hair follicles in SKH1 mice was suggestive of embryonic-like tissue regeneration, a phenomenon not often observed in the murine small wound model.

To further quantify tissue regeneration, we next performed tensile strength testing on unsplinted incisional wounds in SKH1 mice using a modified literature protocol[17]. We found that scar tissue from sham wounds revealed tensile strength that was approximately 15% of unwounded skin from the same animal (Figure 1i). While treatment of wounds with L-MAP hydrogel did not result in a significant increase in tissue tensile strength, treatment with either D or L/D MAP resulted in an ~80% improvement in tensile strength (Figure 1j).

Hair follicles in D-MAP-treated wounds are neogenic.

We next repeated wound healing experiments in B6 mice to investigate if the regenerative phenomenon observed in D-MAP treated wounds was similar to WIHN. We chose sham as control and D-MAP as a treatment method that showed evidence of regeneration in SKH1 mice. Similar to the sham and L-MAP treated wounds in SKH1 mice, the B6 mice wounds without hydrogel (sham) displayed the typical scar appearance by H&E and Masson Trichrome staining (Figure 2a, c, e). In contrast, histological sections of the D-MAP treated tissue revealed clear signs of WIHN. As in SKH1 mice, D-MAP treated B6 mice wounds displayed undulations and numerous epidermal cysts under the epidermis, while the dermis was thicker. Importantly, many neogenic hair follicles developed in the wound (Figure 2b, d, f). The neogenic hair follicles were in early anagen phases with immature appearance, yet

many of them already had formed new sebaceous glands (Figure 2b) and featured prominent $SOX9^+$ bulge stem cell region (Figure 2j). In several instances, neogenic hair follicles were physically connected to epidermal cysts (morphology not expected from pre-existing follicles). This suggests that in D-MAP treated wounds, epidermal cysts can be the initiation sites for *de novo* morphogenesis for at least some of the neogenic hair follicles (Figure 2h). Masson trichrome staining confirmed the presence of neogenic hair follicles within the collagen matrix of the wound bed (Fig 2b, f). Furthermore, regenerating day 18 D-MAP treated wounds with neogenic hair follicles lacked $PLIN^+$ dermal adipocytes (Figure 2h), which is consistent with slower regeneration of neogenic adipocytes that occurs four weeks after wounding in the large wound-induced WIHN[18,19]. Thus, addition of D-MAP to normally non-regenerating 4-mm excisional wounds activates hair follicle neogenesis.

D-MAP hydrogel implants enhance myeloid cell recruitment.

To determine whether an enhanced immune response was leading to enhanced D-MAP or 1:1 L:D MAP degradation in the wound microenvironment, we utilized a subcutaneous implantation model which also allows for larger amounts of hydrogel to be implanted, and thus remain present longer, than in the small excisional wound model. To test whether the subcutaneous implants of D-MAP hydrogel resulted in enhanced immune cell recruitment, we utilized immunofluorescent microscopy with AlexaFluor488 labeled MAP hydrogel. We found that implants containing just L-MAP display a background level of CD11b cells within the hydrogel, as previously observed[1], while D-MAP or L/D-MAP resulted in the robust accumulation of CD11b-expressing myeloid cells within and around the scaffold (Figure 3a–b). Standard histological analysis of a repeat experiment of different formulations of subcutaneously implanted MAP hydrogel confirmed the activation of type 2 immunity with an atypical, type 2 granulomatous response dominated by the accumulation of individual macrophages within and around D-MAP hydrogel implants, but not L-MAP hydrogel implants (see Supplementary Figure 3a and Supplementary Discussion). Immunofluorescent staining for F4/80 and CD11b confirms the enhanced recruitment of macrophages, without giant cell formation, in D-MAP implants (see Supplementary Figure 3b and 3c and Supplementary Discussion). These results confirm that D-MAP elicit a more robust immune response, and degradation by the accumulated immune cells likely contributes to the enhanced degradation of D-MAP in our previous wound experiments.

Allergic responses and parasites can elicit a type 2 immune response including atypical type 2 granulomatous responses at least partially through interleukin (IL)-33 production by epithelial cells, recruited myeloid cells and resident macrophages[20–23]. Implanted, non-degradable microparticle-based materials elicit an IL-33-dependent type 2 innate immune response by circulating $CD11b^+$ myeloid cells and macrophages[24]. It is possible that MAP particles could activate this same program, especially given the atypical type 2 foreign body responses observed in D-MAP samples. Indeed, 21 days after implantation, we found similar numbers of IL-33-expressing $F4/80^+CD11b^+$ macrophages in the center/core of both L- and D-MAP implants (Figure 3c and 3d), consistent with both L- and D-MAP samples activating this type 2 pathway. However, there was a dramatic increase in IL-33 producing $IL\text{-}33^+F4/80^+$ macrophages at the edges of only D-MAP implants (Figure 3c and 3d). These results confirm that the hydrogel possesses a type 2 innate “adjuvant” effect, that may

activate the adaptive immune system and contribute to enhanced immune activation with D-MAP hydrogel. When L-MAP scaffolds are used, the immune response remains mild as the hydrogel degrades slowly over time[25], but the presence of D-peptide accelerates immune mediated degradation.

Free D-chiral peptides avoid pathogen recognition receptors.

We next tested whether D-peptides could directly activate innate immunity through traditional PRR-induced transcriptional response. We stimulated murine bone marrow derived macrophages (BMDMs) with L-peptide or D-peptide in the presence or absence of bacterial lipopolysaccharide (LPS), the Toll-like receptor 4 agonist that results in rapid macrophage transcriptional responses. We chose to examine genes reliably and potently induced downstream of the major signaling pathways downstream of a variety of cellular insult (AP-1, MAPK, NF-κB, and type I IFN) to simultaneously interrogate multiple PRR pathways[26–28]. To our surprise, neither L- nor D-amino acid containing crosslinking peptides alone at high doses (1mg/ml) induced the expression of pro-inflammatory genes *Tnf* (NF-κB dependent), *Il1b* (NF-κB and MAPK dependent), *Cxcl2* (AP-1 dependent early response), or *Mx1* (type I IFN dependent) in murine BMDMs at 6 hours (t_{max} of gene induction; Figure 3e–l). Additionally, neither L- nor D-peptides enhanced the ability of LPS to induce the expression of these same genes (Figure 3e–h).

Previous studies have shown that peptides containing an N-terminal D-methionine can activate the innate immune receptor formyl peptide receptor 2 and formyl peptide like receptor 2[29–31]. Since cleavage of D-amino acid peptide can result in shorter peptides that contain a D-amino acid at the N-terminus, we next wished to examine whether a peptide corresponding to the cleaved D-peptide could activate inflammatory responses in BMDMs. Similar to the results with intact D-peptide, high concentrations of cleaved D-peptide (1mg/ml) did not induce the transcription of *Tnf*, *Il1b, Cxcl2*, or *Mx1* at 6 hours (Figure 3i–l). Since there is a very low likelihood that cleaved D-peptide will be present at such high local concentrations within the implanted hydrogel while it is being degraded *in vivo*, these show that D-chiral peptides are poor activators of a traditional PRR-mediated inflammatory response in macrophages and suggest that D-peptides may be acting as antigens to enhance immunity, leading to enhanced degradation of D-MAP.

D-MAP elicits antigen-specific humoral immunity.

We next evaluated whether the D-MAP activates adaptive immunity. The adaptive immune system recognizes non-self-peptide antigens to induce cell mediated (T cell) and humoral (B cell) immunity. Peptides containing D-amino acids have been reported to activate or suppress T cell dependent and T cell independent adaptive immune responses[5,32]. In the context of the MAP, cross-linking peptides that are non-native may be presented to the immune system until fully degraded. D-peptides could be presented by antigen presenting cells directly to T cells, eliciting a T cell dependent adaptive immune response or alternatively, the presence of D-amino acid containing peptides on the surface of a large molecule of MAP hydrogel could directly crosslink the B cell receptor, leading to T cell independent antibody responses similar to T cell independent antigens. To test this

hypothesis, we examined whether mice that were wounded or received subcutaneous implants of L-MAP, D-MAP, or 1:1 L/D-MAP were able to develop T-helper cell dependent (IgG1 or IgG2a) or T cell independent (IgG3) antibodies against L- or D- amino acid containing crosslinkers[33–36].

Indeed, regardless of whether D-containing MAP hydrogel was applied to wounded tissue or given via subcutaneous implants, mice developed a T cell dependent IgG1 and IgG2a response against the D-amino acid containing peptide, but not a T cell independent IgG3 response. These results are more consistent with a T cell-dependent immune response against D-peptides (Figure 4a–b). IgG1 is typically associated with a Th2 “tissue repair” type response, while IgG2a is typically associated with a Th1 “foreign body” response that typically requires strong adjuvants to develop, depending on the strain of mice[37,38]. The fact that anti-D peptide-specific IgG2a induced when the hydrogel was given to mice in a wound environment but not when the hydrogel was given in the subcutaneous implant model suggests that, by itself, the hydrogel does not possess sufficient adjuvant effects to induce robust Th1 responses. However, the inflammation present in the wound environment may result in a mixed Th2/Th1 response to the D-MAP (Figure 4b and 3e). Mice that were treated with L-MAP alone did not develop antibody responses to L-peptide.

D-MAP recruits myeloid cells via adaptive immune response.

Our data suggest that the activation of adaptive immune responses to D-MAP contributes to immune infiltration and degradation of D-MAP. To test this hypothesis further, we examined whether Balb/c.Rag2$^{-/-}\gamma c^{-/-}$ mice, which are devoid of an adaptive immune system, innate lymphoid cells, and IL-2/IL-15 signaling, but possess a fully functional myeloid system, will exhibit reduced immune infiltration[39]. Indeed, total cellularity and the specific recruitment of CD11b^{+} myeloid cells to D-MAP hydrogel in Balb/c.Rag2$^{-/-}\gamma c^{-/-}$ mice were decreased to comparable levels to those seen in L-MAP in WT mice (Figure 4k–l).

D-MAP-induced skin regeneration relies on adaptive immunity.

To determine whether the adaptive immune response was required for the development of neogenic hair follicles, we next performed excisional splinted wounds in B6 and B6.Rag1$^{-/-}$ mice, and examined them 25 days after wounding with untreated (sham) or treated wounds with 1:1 L/D-MAP gel. Of note, because in preliminary studies, scars induced by 4-mm punch wounds healed with extremely small scars in B6 mice, we used a 6-mm punch in this experiment.

Sham wounds in B6 mice demonstrated an obvious depigmented, irregularly-shaped scar, while scars in B6 mice treated with 1:1 L/D-MAP gel were difficult to identify visually as they displayed hair growth over the wounds and less atrophy/surface changes typically seen in scars (representative example Figure 5a, all wound images Supplementary Figure 4). Scars in sham-treated or 1:1 L/D-MAP-treated B6.Rag1$^{-/-}$ mice were smaller than those in sham-treated B6 mice, but were identifiable in B6.Rag1$^{-/-}$ mice regardless of whether wounds were sham treated or hydrogel treated (Figure 5a). All wound (including 1:1 L/D-MAP-treated B6 wound areas) injuries were confirmed by examining the defect on the

fascial side of the tissue after excision of skin. Histological sections of the healed skin of mice displayed significant neogenic hairs and sebaceous glands only in wounds of wildtype mice treated with 1:1 L/D-MAP (Figure 5b–d, and Supplementary Figure 5). Sham wounds in B6 and Rag$^{-/-}$ mice, and in the 1:1 L/D-MAP treated B6.Rag1$^{-/-}$ mice displayed prominent scars, without hairs or sebaceous glands, confirming the requirement of adaptive immune system in skin regeneration by D-peptide containing MAP gel (Figure 5b–d). These studies highlight that hair follicle structures can be regenerated through adaptive immune activation from MAP hydrogel scaffolds.

Discussion

In most mammals, the natural process of scar formation and tissue fibrosis is highly evolved and is a tissue-scale attempt to restore critical barrier functions for survival. This process, however, is ultimately a biological ‘triage’ that favors the rapid deposition of a fibrotic matrix to restore the barrier at the expense of a loss of function of complex tissue. In the skin, this fibrotic response results not only in a loss of functioning adnexal structures, but skin tissue that is more fragile and prone to re-injury. A major goal when engineering skin regeneration is to allow for the rapid restoration of barrier function while providing increased tissue tensile strength and higher tissue function. Many biomaterial-based approaches including addition of growth factors and decellularized extracellular matrix constructs display limited success in restoring function in wounds. We previously showed that the MAP scaffold can accelerate wound closure in murine wounds[1]. Our findings reported here further highlight that incorporation of a modest adaptation to MAP that enhanced a type 2 innate and adaptive immune response, induced skin regeneration: hair neogenesis and improved tensile strength (Figure 6). This response was dependent upon the generation of an adaptive immune response to D-enantiomeric peptides, and occurred without addition of stem cells, growth factors, or adjuvants. Importantly, this regenerative response was decoupled from wound closure that begins immediately, consistent with the time needed to generate an antigen specific immune response.

While adaptive immunity can contribute to fibrosis, foreign body formation, and rejection of biomaterial implants[6–8], adaptive immune activation from growth factor containing extracellular matrices can enhance muscle regeneration[8,9]. Further, other biomaterials were created to directly activate specific components of the immune system to treat cancer as immunotherapy platforms[40,41]. In concert, these studies suggest that the role of the adaptive immune system in tissue repair is significantly more complex than previously realized. Our findings suggest that an engineered type 2 immune response to sterile, degradable microparticle-based materials can trigger regeneration rather than fibrosis and further support a role of adaptive immune cells to restore tissue function. Finally, we display the potential of the MAP scaffold as a potent immunomodulatory platform. Future identification of immune factors that tip the balance towards regeneration rather than eliciting scarring or a foreign body response may lead to improved biomaterials.

Methods

L-MMP and D-MMP MAP Hydrogel Formation.—Microfluidic water-in-oil droplet generators were fabricated using soft lithography, as previously described[1]. To enable microgel formation, two aqueous solutions were prepared. One solution contained a 10% w/v 4-arm PEG-vinyl sulfone (20 kDa, JenKem USA) in 300 mM triethanolamine (Sigma), pH 8.25, pre-functionalized with 500μM K-peptide (Ac-FKGGERCG-NH2) (GenScript), 500 μM Q-peptide (AcNQEQVSPLGGERCG-NH2), and 1 mM RGD (Ac-RGDSPGERCG-NH2) (GenScript). The other solution contained an 8mM di-cysteine modified Matrix Metalloprotease (MMP) (Ac-GCRDGPQGIWGQDRCG-NH2) (GenScript) substrate with either all L-chirality amino acid residues for L-MMP microgels or D-chirality amino acid substitution of amino acids at the site of MMP-mediated recognition and cleavage (Ac-GCRDGPQ_DGI_DW$_D$GQDRCG-NH2) for D-MMP microgels. We matched the stiffness of the two hydrogels which required minimal changes to peptide crosslinker solution (L-MAP – 8mM; D-MAP – 8.2mM). The oil phase was a heavy mineral oil (Fisher) containing 0.25% v/v Span-80 (Sigma). The two solutions were mixed in the droplet generator and pinched immediately into monodisperse droplets. Downstream of the pinching region, a second oil inlet with a high concentration of Span-80 (5% v/v) was mixed with the flowing droplet emulsion. Both aqueous solution flow rates used were 0.75 μL/min, while both oil solutions were flowed at 4μL/min. The mixture was allowed to react overnight at room temperature and purified by repeated washes with an aqueous buffer of HEPES buffered saline pH 7.4 and pelleting in a tabletop centrifuge at 18000 × g for 5 mins. Raw materials are purchased endotoxin free and the final hydrogels are tested for endotoxin levels prior to implantation.

Generation of MAP scaffolds from building block μgels—Fully swollen and equilibrated building block μgels were pelleted at 18000 × g for five minutes, and the excess buffer (HEPES pH 7.4 + 10 mM CaCl2) was removed by aspiration. Subsequently, building blocks were split into aliquots, each containing 50 μl of concentrated building blocks. An equal volume of HEPES pH 7.4 + 10 mM CaCl2 was added to the concentrated building block solutions. Half of these are spiked with Thrombin (Sigma) to a final concentration of 2 U/ml and the other half spiked with FXIII (CSL Behring) to a final concentration of 10 U/ml. These solutions were then well mixed and spun down at 18000 × g, followed by removal of excess liquid with a cleanroom wipe (American Cleanstat).

Annealing was initiated by mixing equal volumes of the building block solutions containing Thrombin and FXIII using a positive displacement pipet (Gilson). These solutions were well mixed by pipetting up and down, repeatedly, in conjunction with stirring using the pipet tip. The mixed solution was then pipetted into the desired location (mold, well plate, mouse wound, etc.) or loaded into a syringe for subcutaneous injection. The microgel fabrication was performed under sterile conditions. Following particle fabrication, 20 ul of dry particles were digested in 200 ul digestion solution (Collagenase IV 200 U/ml+ DNase I 125U/ml) and incubated in 37 C for 30 min before testing. Endotoxin concentrations were determined with Pierce LAL Chromogenic Endotoxin Quantitation Kit (Thermo Fisher Scientific)

following manufacturer's instructions. Particle Endotoxin levels were consistently below 0.2 Endotoxin U/mL.

Degradation with collagenase—Microgel degradability was confirmed with collagenase I. A 1:1 v/v mixture of microgels formed with MMP-D- or MMP-L-sensitive cross-linker was diluted in collagenase I to a final concentration of 5 units collagenase/mL. This mixture was added to a 1 mm PDMS well and briefly allowed to settle. Images of the microgels were taken near the bottom of the well every 30 seconds for 2 hours with a confocal microscope. Image analysis was carried out through a custom MATLAB script (script provided by Dr. Sasha Cai Lesher-Perez) and ImageJ. MATLAB was used to determine the number of intact microgel spheres in each image. The previously mentioned script was applied with a minimum droplet radius of 30 pixels, a maximum droplet radius of 50 pixels, and a sensitivity factor of 0.98 for channel-separated images. Then, ImageJ was used to determine the area fraction fluorescing for each channel and each image. The thresholding for each image was set to a minimum of 50 and a maximum of 255 and the fluorescing area fraction was recorded.

Mouse excisional wound healing model—All experiments involving animals, animal cells or tissues were performed in accordance to the Chancelor's Animal Research Committee (ARC) ethical guidelines at UCLA under protocol # 10–011 (in vivo wound healing and subcutaneous implants) or # 1999–073 (in vitro BMDM cultures). Mouse excisional wound healing experiments were performed as previously described[1,10]. Briefly 10-week old female SKH1 mice (Charles River Laboratories; n=6), or 10-week old female C57Bl/6 (B6) or B6.Rag1$^{-/-}$ mice (Jackson Laboratories; n=4 twice) were anesthetized using continuous application of aerosolized isoflurane (1.5 vol%) throughout the duration of the procedure and disinfected with serial washes of povidone-iodine and 70% ethanol. The nails were trimmed and buprenorphine 0.05mg/ml) was injected intramuscularly. The mice were placed on their side and dorsal skin was pinched along the midline. A sterile 4 mm biopsy punch was then used to create 2 through-and-through wounds, resulting in four clean-cut, symmetrical, full-thickness excisional wounds on either side of the dorsal midline. A small amount of adhesive (VetBond, 3M, Inc.) was then applied to one side of a rubber splint (O.D. ~12mm; I.D. ~8mm) and the splint was placed centered around the wound (adhesive side down). The splint was secured with eight interrupted sutures of 5–0 non-absorbable Prolene. A second splint wrapped in Tegaderm (3M, Inc.) was attached to the initial splint via a single suture to act as a hinged cover to allow wound imaging while acting as a physical barrier above the wound bed. After addition of thrombin (2 U/ml) and 10mM $CaCl_2$, the experimental material (20 μL of L-only MAP, D-only MAP, 1:1 v/v mixture of L-MAP and D-MAP in HEPES-buffered saline containing Factor XIII (10U/ml) and 10mM CaCl2, or no hydrogel) was then added to one of the wound beds randomly to ensure each hydrogel treatment was applied to the different regions of wounded back skin to limit potential for site-specific effects. Following treatment, a Tegaderm-coated splint was applied, and wound sites were covered using a self-adhering elastic bandage (VetWrap, 3M, Inc.). Animals were housed individually to prevent wound manipulation. At the culmination of the wound healing experiment (Day 21 or Day 25) the mice were sacrificed by isoflurane overdose and cervical dislocation and imaged with a digital camera. The skin was excised

and processed via either paraffin embedding for H&E or OCT blocks for immunofluorescence.

Evaluation of wound closure—Wounds were imaged daily to follow closure of the wounds. Each wound site was imaged using high-resolution camera (Nikon Coolpix). Closure fraction was determined as described previously[1]. Briefly, closure was determined by comparing the pixel area of the wound to the pixel area within the 10 mm center hole of the red rubber splint. Closure fractions were normalized to Day 0 for each mouse/scaffold sample. Investigators were blinded to treatment group identity during analysis.

Wound Imaging—On the specified day after wounds were created, close up images of wounds were taken using a Canon Powershot A2600 or a Nikon D3400 DSLR Camera with an 18–55mm Lens, and were cropped to the wound area but not manipulated further. For wound closure, area was obtained using ImageJ by a subject blinded to the treatment.

Tissue collection—After wounds healed, mice were sacrificed on the indicated day after wounding, and tissue collected with a ~5mm margin around healed wound. The samples were immediately submerged in Tissue-Tek Optimal Cutting Temperature (OCT) fluid and frozen into a solid block with liquid nitrogen. The blocks were then cryo-sectioned by cryostat microtome (Leica) and kept frozen until use. The sections were then fixed with 4% paraformaldehyde in 1X PBS for 30 minutes at room temperature, washed with 1X PBS, and kept at 4°C until stained. For antibody production analysis, blood harvested via cardiac puncture to obtain serum for ELISA.

Macrophage cell culture—Mouse bone marrow derived macrophages were generated as previously described previously[27]. Briefly, following euthanasia, hindlimbs were removed aseptically and bone marrow was flushed. Bone marrow cells were cultured in CMG-conditioned complete DMEM media for 6 days. Cells were then treated with intact L-or D-peptide in ultra-pure H_20 at the indicated concentration in the presence or absence of LPS (10ng/ml). Cleaved D-peptide (with an N-terminal D-amino acid) ($W_DGQDRCG$-NH2) was also used when indicated. Cells were harvested at 6 hours following treatment and expression of cytokines and chemokines was examined by qPCR using specific primers as described previously[42].

Incisional wound model—10-week old female C57Bl/6 mice (Jackson Laboratories) were anesthetized with isoflurane as above. The dorsal and side skin was dehaired using electric clippers followed by Nair (Church and Dwight, Inc.), then disinfected with serial washes of povidone-iodine and 70% ethanol. The nails were trimmed to lower the incidence of splint removal, and buprenorphine was injected IM as above. An incisional 2cm × 1cm wound was made with a scalpel. Mice (5 per group) were randomly assigned to receive 50μL of L-MAP, D-MAP, 1:1 v/v mixture of L-MAP and D-MAP or no hydrogel (aquafor). The mice were wrapped with Tegaderm followed by VetWrap as above.

Histology and analysis.—Samples were sectioned (6–10μm thick), then stained with hematoxylin and eosin or Masson trichrome by the UCLA Tissue Procurement Core Laboratory using standard procedures. Sections were examined by a board certified

dermatopathologist (P.O.S.) and/or an expert in hair follicle neogenesis/regeneration (M.V.P.) who were blinded to the identity of the samples, for the presence of adnexal structures in tissue sections and dermal thickness. For enumeration, two to three tissue sections from the tissue block of each wound were examined and averaged per wound to obtain the count per unit area for each sample. Wounds were splinted to prevent contraction and any sample with more than 50% wound closure by contraction were not included.

Tensiometry.—To evaluate the tensile properties of the healed incisional wounds, tensile testing was performed on an Instron model 3342 fitted with a 50N load cell and data recorded using the Instron Bluehill 3 software package. Tissue was collected from the wound site 28 days following wounding/treatment as a 2 cm × 4 cm "dumbbell" shape (with 1 cm center width in the handle portion). The sample was oriented such that the healed wound spanned the entire middle section of the dog bone (the thinner 1cm region) and the healed wound long axis was orthogonal to the direction of tension applied. The tissue sample was loaded into the Instron and secured with pneumatic gripers, pressurized to 40 PSI. The tissue was subjected to tensile testing at an elongation rate of 5 mm/min and ran through material failure.

For each tissue sample, stress/strain curves were calculated from force/elongation curves (provided from the Instron Bluehill software) using the known cross-sectional dimensions of the "dog bone" samples (each measured with calipers prior to placement on the Instron), and by measuring the starting distance between pneumatic grips with a caliper. The starting distance was standardized by preloading the sample to 0.5N, followed by measurement and then running of the tensile test to failure. This analysis enabled calculation of Yield Stress, which are reporting in Figure 1j.

Subcutaneous implants of hydrogel—For subcutaneous implants, after anesthesia, 10-week old female Balb/c and Balb/c.Rag2$^{-/-}\gamma c^{-/-}$ mice were injected with 50μL of L-MAP, D-MAP, or 1:1 v/v mixture of L-MAP and D-MAP (n = 5). 21 days later the skin and subcutaneous tissue containing the hydrogels were removed and processed for histology and immunofluorescence, and blood was collected by cardiac puncture to obtain serum for ELISA. B6 mice were used in another batch of experiments for immunofluorescence analysis and histology of subcutaneous implants.

Tissue section Immunofluorescence, quantification of hydrogel degradation, and immune infiltration.—Slides containing tissue sections (10–25 μm thickness) were blocked with 3% normal goat serum (NGS) in 1X PBS + 0.05% Tween-20 (PBS-T). For intracellular antigens 0.2% triton was added to the blocking buffer. Primary antibody dilutions were prepared as follows in 5% NGS in 1X PBST: rat anti mouse CD11b clone M1–70 (BD Pharmingen; #553308) – 1:100, F4/80 clone A3–1 (BioRAD; MCA497G) – 1:400, and IL-33 (abcam; ab187060) – 1:200. Sections were stained with primary antibodies overnight at 4°C, and subsequently washed with 3% NGS in 1X PBS-T. Secondary antibodies (Goat anti-rat Alexa-647, Invitrogen) were all prepared in 5% Normal Goat Serum (NGS) in 1X PBST at a dilution of 1:500. Three 5-minute washes with PBST were performed after each antibody incubation. Sections were incubated in secondary antibodies for 1 hour at room temperature, and subsequently washed with 1X PBST. For multicolor

immunofluorescence staining for primary and secondary of each antigen were performed in sequence. Sections were either mounted with antifade mounting medium with DAPI (Fisher Scientific; H1200) or counterstained with 2 μg/ml DAPI in 1X PBST for 30 mins at room temperature and then mounted in Antifade Gold mounting medium.

Computational analysis of multi-color immunofluorescence images—A MATLAB code was used for analysis of the multicolor immunofluorescence images. The code divides the hydrogel into an Edge region (300um from hydrogel-tissue interface) and a Core region (the center of hydrogel to 200um from the inner boundary of the Edge region). For each hydrogel subregion the code reads CD11b and F4/80 signal, binarizes each to form a mask using a similar threshold for all samples. The code then uses the nuclear stain and IL-33^{+} stains to identify all nuclei and IL-33^{+} cells. The density of each cell type is then quantified by counting the number of nuclei and IL-33^{+} cells overlapping or evading the masks divided by the area of the region of interest. Areas with defects caused by tissue sectioning were excluded from analysis. Although not affecting the code performance, the image condition was kept the same across all samples.

ELISA—For assessment of anti-L or anti-D antibodies, sera were collected by cardiac puncture 21 days following hydrogel application of mice (subcutaneous implant or application to wound). for detection of anti-L and anti-D antibodies plates were coated with either L-MMP peptide or D-MMP peptide respectively (GenScript; sequence above) Serum samples were tested at a 1:500 dilution followed by incubation with alkaline phosphatase-labeled goat anti-mouse IgG1 or IgG2a, or IgG3 antibodies (Southern Biotechnology Associates or BD Pharmingen), and development with *p*-nitrophenylphosphate substrate (Sigma-Aldrich). Optical density at 405 nm (OD_{405}) was read using a spectramax i3X microplate reader (Softmax Pro 3.1 software; Molecular Devices).

Statistics and Reproducibility

All statistical analysis was performed using Prism 6 (GraphPad, Inc.) software. Specifically, two-tailed t-test or one-way ANOVA were used to determine statistical significance, assuming equal sample variance for each experimental group when comparing individual groups. For ANOVA, post hoc analysis with Tukey multiple comparison. For histological counting, B6 and B6.Rag1$^{-/-}$ sham vs 1:1 L/D-MAP analysis, Wilcoxon signed rank analysis was performed, and B6 vs B6.Rag1$^{-/-}$ and subcutaneous immunofluorescence analysis was performed with t test with Mann-Whitney U test.

The hydrogel degradation test was performed on three separate occasions for each batch of L-MAP, D-MAP, and a 50:50 mixture of L-MAP and D-MAP for a total of nine degradation tests. In each technical replicate at least 10 microgels were imaged and analyzed for fluorescence intensity.

The evaluation of hair neogenesis in B6 mice Control vs D-MAP for Figure 2 was performed on samples from n= 4 for each group. The wound healing studies comparing WT to Rag1$^{-/-}$ mice were repeated three times (n=4 each group). In the first experiment, all Rag1−/− mice were euthanized due to the development of severe and worsening wound infections, and thus were not included in the final analysis. In addition, wounds/scars that

showed more than 50% contraction of the wound area from the underlying fascia from any group were removed from the final data set or if the histological processing failed to identify the wound/scar bed (i.e. sample was cut through). For the histological analysis, Sham vs 1:1 L/D in B6 mice from 3 separate experiments was used (n=9 histological samples available out of an available n=12 wounds performed), while samples in the B6.Rag1$^{-/-}$ mice were obtained from the latter two experiments performed in B6 vs B6.Rag1$^{-/-}$ mice performed at the same time (n=6 histological samples available out of an n=8 wounds. The findings within this manuscript were observed in two different mouse strains (CRL-SKH and C57Bl/6) that have different adnexal structures (vellus hair only and mature/terminal follicles, respectively).

Data Availability

The data that support the findings of this study are available from the corresponding authors upon reasonable request.

Supplementary Material

Refer to Web version on PubMed Central for supplementary material.

Acknowledgements

We would like to thank the National Institutes of Health for funding F32EB018713-01A1 (DRG), T32-GM008042 (MMA), U01AR073159 (MVP), R01NS094599 (TS), R01HL110592 (TS), R03AR073940 (POS), K08AR066545 (POS), Pew Charitable Trust (MVP), LEO Foundation (MVP), NSF grant DMS1763272, and Simons Foundation Grant (594598, QN) (MVP). We would like to thank Dr. Sasha Cai Lesher-Perez and Michael Bogumil for their assistance with MATLAB coding. We like to thank Yining Liu for assistance running endotoxin texts. We would also like to thank the Advanced Light Microscopy and Spectroscopy at California NanoSystems Institute and Electron Microscopy Core Laboratory of the Brain Research Institute at UCLA and, particularly, for the significant help of Marianne Cilluffo.

References

1. Griffin DR, Weaver WM, Scumpia P, Di Carlo D & Segura T Accelerated wound healing by injectable microporous gel scaffolds assembled from annealed building blocks. Nat. Mater 14, 737–744 (2015). [PubMed: 26030305]
2. Nih LR, Sideris E, Carmichael ST & Segura T Injection of Microporous Annealing Particle (MAP) Hydrogels in the Stroke Cavity Reduces Gliosis and Inflammation and Promotes NPC Migration to the Lesion. Adv. Mater. Deerfield Beach Fla 29, (2017).
3. Xu Q et al. Injectable hyperbranched poly(β-amino ester) hydrogels with on-demand degradation profiles to match wound healing processes. Chem. Sci 9, 2179–2187 (2018). [PubMed: 29719691]
4. Zhu S, Nih L, Carmichael ST, Lu Y & Segura T Enzyme-Responsive Delivery of Multiple Proteins with Spatiotemporal Control. Adv. Mater. Deerfield Beach Fla 27, 3620–3625 (2015).
5. Sela M & Zisman E Different roles of D-amino acids in immune phenomena. FASEB J. Off. Publ. Fed. Am. Soc. Exp. Biol 11, 449–456 (1997).
6. Doloff JC et al. Colony stimulating factor-1 receptor is a central component of the foreign body response to biomaterial implants in rodents and non-human primates. Nat. Mater 16, 671–680 (2017). [PubMed: 28319612]
7. Mishra PK et al. Sterile particle-induced inflammation is mediated by macrophages releasing IL-33 through a Bruton's tyrosine kinase-dependent pathway. Nat. Mater 18, 289–297 (2019). [PubMed: 30664693]

8. Chung L, Maestas DR, Housseau F & Elisseeff JH Key players in the immune response to biomaterial scaffolds for regenerative medicine. Adv. Drug Deliv. Rev 114, 184–192 (2017). [PubMed: 28712923]
9. Sadtler K et al. Developing a pro-regenerative biomaterial scaffold microenvironment requires T helper 2 cells. Science 352, 366–370 (2016). [PubMed: 27081073]
10. Galiano RD, Michaels J, Dobryansky M, Levine JP & Gurtner GC Quantitative and reproducible murine model of excisional wound healing. Wound Repair Regen. Off. Publ. Wound Heal. Soc. Eur. Tissue Repair Soc 12, 485–492 (2004).
11. Ito M et al. Wnt-dependent de novo hair follicle regeneration in adult mouse skin after wounding. Nature 447, 316–320 (2007). [PubMed: 17507982]
12. Seifert AW et al. Skin shedding and tissue regeneration in African spiny mice (Acomys). Nature 489, 561–565 (2012). [PubMed: 23018966]
13. Nelson AM et al. dsRNA Released by Tissue Damage Activates TLR3 to Drive Skin Regeneration. Cell Stem Cell 17, 139–151 (2015). [PubMed: 26253200]
14. Guerrero-Juarez CF et al. Wound Regeneration Deficit in Rats Correlates with Low Morphogenetic Potential and Distinct Transcriptome Profile of Epidermis. J. Invest. Dermatol 138, 1409–1419 (2018). [PubMed: 29317265]
15. Marshall CD et al. Sanativo Wound Healing Product Does Not Accelerate Reepithelialization in a Mouse Cutaneous Wound Healing Model. Plast. Reconstr. Surg 139, 343–352 (2017). [PubMed: 28121865]
16. Lim CH et al. Hedgehog stimulates hair follicle neogenesis by creating inductive dermis during murine skin wound healing. Nat. Commun 9, 4903 (2018). [PubMed: 30464171]
17. Carlson MA & Chakkalakal D Tensile properties of the murine ventral vertical midline incision. PloS One 6, e24212 (2011). [PubMed: 21915298]
18. Plikus MV et al. Regeneration of fat cells from myofibroblasts during wound healing. Science 355, 748–752 (2017). [PubMed: 28059714]
19. Guerrero-Juarez CF et al. Single-cell analysis reveals fibroblast heterogeneity and myeloid-derived adipocyte progenitors in murine skin wounds. Nat. Commun 10, 650 (2019). [PubMed: 30737373]
20. Warren KS A functional classification of granulomatous inflammation. Ann. N. Y. Acad. Sci 278, 7–18 (1976). [PubMed: 786128]
21. Chensue SW et al. Cytokine responses during mycobacterial and schistosomal antigen-induced pulmonary granuloma formation. Production of Th1 and Th2 cytokines and relative contribution of tumor necrosis factor. Am. J. Pathol 145, 1105–1113 (1994). [PubMed: 7977642]
22. Wills-Karp M et al. Trefoil factor 2 rapidly induces interleukin 33 to promote type 2 immunity during allergic asthma and hookworm infection. J. Exp. Med 209, 607–622 (2012). [PubMed: 22329990]
23. Hardman CS, Panova V & McKenzie ANJ IL-33 citrine reporter mice reveal the temporal and spatial expression of IL-33 during allergic lung inflammation. Eur. J. Immunol 43, 488–498 (2013). [PubMed: 23169007]
24. de Kouchkovsky DA, Ghosh S & Rothlin CV Induction of sterile type 2 inflammation. Nat. Mater 18, 193–194 (2019). [PubMed: 30783225]
25. Koh J et al. Enhanced In Vivo Delivery of Stem Cells using Microporous Annealed Particle Scaffolds. Small Weinh. Bergstr. Ger 15, e1903147 (2019).
26. Purbey PK et al. Defined Sensing Mechanisms and Signaling Pathways Contribute to the Global Inflammatory Gene Expression Output Elicited by Ionizing Radiation. Immunity 47, 421–434.e3 (2017). [PubMed: 28930658]
27. Scumpia PO et al. Opposing roles of Toll-like receptor and cytosolic DNA-STING signaling pathways for Staphylococcus aureus cutaneous host defense. PLoS Pathog. 13, (2017).
28. Tong A-J et al. A Stringent Systems Approach Uncovers Gene-Specific Mechanisms Regulating Inflammation. Cell 165, 165–179 (2016). [PubMed: 26924576]
29. Kim SD et al. The agonists of formyl peptide receptors prevent development of severe sepsis after microbial infection. J. Immunol. Baltim. Md 1950 185, 4302–4310 (2010).

30. Kang HK et al. The synthetic peptide Trp-Lys-Tyr-Met-Val-D-Met inhibits human monocyte-derived dendritic cell maturation via formyl peptide receptor and formyl peptide receptor-like 2. J. Immunol. Baltim. Md 1950 175, 685–692 (2005).
31. Schepetkin IA et al. 3-(1H-indol-3-yl)-2-[3-(4-nitrophenyl)ureido]propanamide enantiomers with human formyl-peptide receptor agonist activity: molecular modeling of chiral recognition by FPR2. Biochem. Pharmacol 85, 404–416 (2013). [PubMed: 23219934]
32. Zisman E, Dayan M, Sela M & Mozes E Ia-antigen-T-cell interactions for a thymus-independent antigen composed of D amino acids. Proc. Natl. Acad. Sci. U. S. A 90, 994–998 (1993). [PubMed: 8381541]
33. Cernysiov V, Gerasimcik N, Mauricas M & Girkontaite I Regulation of T-cell-independent and T-cell-dependent antibody production by circadian rhythm and melatonin. Int. Immunol 22, 25–34 (2010). [PubMed: 19946015]
34. Honda S et al. Enhanced humoral immune responses against T-independent antigens in Fc alpha/muR-deficient mice. Proc. Natl. Acad. Sci. U. S. A 106, 11230–11235 (2009). [PubMed: 19549827]
35. Mongini PK, Stein KE & Paul WE T cell regulation of IgG subclass antibody production in response to T-independent antigens. J. Exp. Med 153, 1–12 (1981). [PubMed: 6969777]
36. Weinstein JS et al. Maintenance of anti-Sm/RNP autoantibody production by plasma cells residing in ectopic lymphoid tissue and bone marrow memory B cells. J. Immunol. Baltim. Md 1950 190, 3916–3927 (2013).
37. Germann T et al. Interleukin-12 profoundly up-regulates the synthesis of antigen-specific complement-fixing IgG2a, IgG2b and IgG3 antibody subclasses in vivo. Eur. J. Immunol 25, 823–829 (1995). [PubMed: 7705414]
38. Boehler RM, Graham JG & Shea LD Tissue engineering tools for modulation of the immune response. BioTechniques 51, 239–240, 242, 244 passim (2011). [PubMed: 21988690]
39. Song J et al. A mouse model for the human pathogen Salmonella typhi. Cell Host Microbe 8, 369–376 (2010). [PubMed: 20951970]
40. Park CG et al. Extended release of perioperative immunotherapy prevents tumor recurrence and eliminates metastases. Sci. Transl. Med 10, (2018).
41. Kim J et al. Injectable, spontaneously assembling, inorganic scaffolds modulate immune cells in vivo and increase vaccine efficacy. Nat. Biotechnol 33, 64–72 (2015). [PubMed: 25485616]
42. Ramirez-Carrozzi VR et al. A unifying model for the selective regulation of inducible transcription by CpG islands and nucleosome remodeling. Cell 138, 114–128 (2009). [PubMed: 19596239]

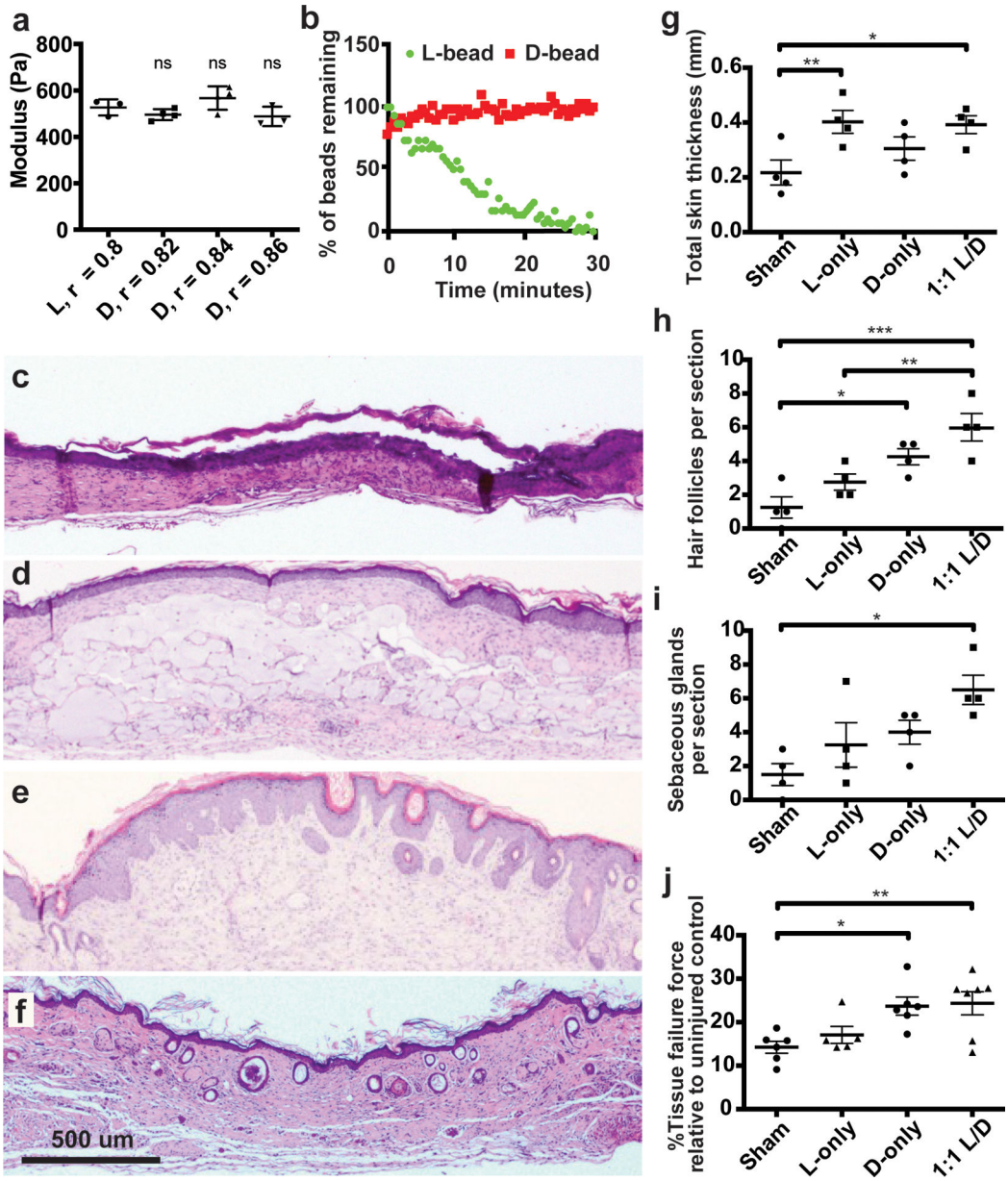

Figure 1. D-MAP hydrogel degradation is enhanced in wounds of SKH1 hairless mice.

a) Rheological characterization of MAP hydrogels composed of L or D-peptide crosslinked microgels. The r-ratio (ratio of -SH to -VS) used to form the microgels was changed to arrive at the same storage modulus for both L and D MAP scaffolds. NS represents a no statistical significance between the L MAP scaffold to the D-MAP scaffold indicated using a two-tailed student t-test. **b**) Fabricated L or D hydrogels were tested for *in vitro* enzymolysis behavior through exposure to a solution of collagenase I (5U/mL). **c-f**) Representative low power view of H&E sections from healed skin 21 days after splinted excisional wounding from a Sham (c), L-MAP (d), D-MAP (e), and 1:1 mixture of L-MAP and D-MAP treated wound in SKH1 mice (f). **g-i**) Histologic quantification of dermal thickness including gels (in mm), hair follicles, and sebaceous glands. Each point represents average of 2 sections from 2 separate slides of one wound. Each data point represents one animal and all analysis

is by one-way ANOVA (respective F-values (3,12): 4.448, 10.89, 5.074, stars denote statistical significance by Tukey multiple comparisons test: g) *p=0.0460, **p=0.0341, h) *p=0.0220, **p= 0.0133, ***p=0.0007 i) *p=0.0110). **j**) 28 days after incisional, unsplinted wounds were created, healed wounds that were treated without or with different hydrogels were tested against unwounded skin in the same mouse. Tensile strength was evaluated by tensiometry and reported as a percentage of the tensile strength of the scar tissue when compared to the normal skin of the same mouse. Each data point represents average of two measurement from one wound, separate from wounds used in b-i with analysis by one-way ANOVA (F-value (3, 20): 5.400, *p=0.0273, **p=0.0131). Data is plotted as a scatter plot showing the mean and standard deviation.

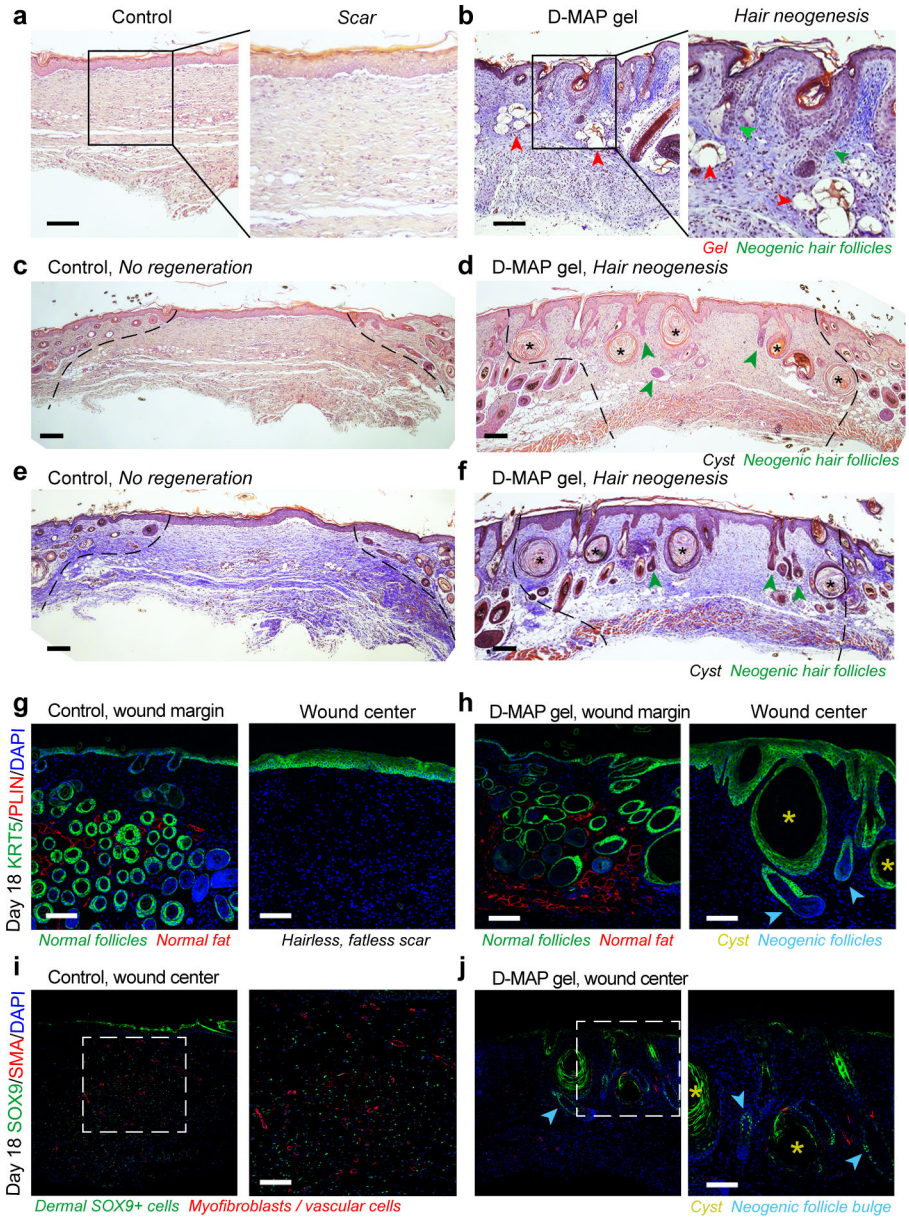

Figure 2: D-MAP hydrogel induces neogenesis of hair follicles in full-thickness skin wounds in B6 mice.

a-f) H&E (a, c, d) and Trichrome staining (b, e, f) of healed 4-mm full-thickness splinted skin wound on day 18. Control (sham-treated) wounds heal with scarring (a, c, e), while D-MAP gel treated wounds form numerous epidermal cysts (asterisks) and, prominently, regenerate *de novo* hair follicles (green arrowheads) (b, d, f). In some instances, neogenic hair follicles form in close association with epidermal cysts. As compared to normal, pre-existing anagen hair follicles at the wound edges, neogenic hair follicles display early anagen stage morphology (Wound edges in b-d are outlined and D-MAP hydrogel remnants in b are marked with red arrowheads). **g-h**) Immunostaining for epithelial marker KRT5 (green) and adipocyte marker PLIN (red), reveals normal $KRT5^{+}$ anagen hair follicles and many mature $PLIN^{+}$ dermal adipocytes (left panels in g and h). Regeneration of new KRT5+

hair follicles (arrowheads in h) along with KRT5+ epidermal cysts is observed only in D-MAP hydrogel-treated wounds (right panel g vs. h). No neogenic adipocytes are observed in hair-forming D-MAP-treated wounds. **i-j**) Immunostaining for SOX9 (green) and SMA (red), reveals many $SOX9^{+}$ epithelial cells within the bulge region of neogenic hair follicles in day 18 DMAP-treated wounds (arrowheads in j). In contrast, in control (sham-treated) wounds that undergo scarring, dermal wound portion contains many $Sox9^{+}$ cells, many of which also co-express contractile marker SMA (i). Expression of SMA is also seen in both control and D-MAP-treated samples in blood vessels. Scales in a-j = 100 μm. The images are representative of slides from 4 animals per group.

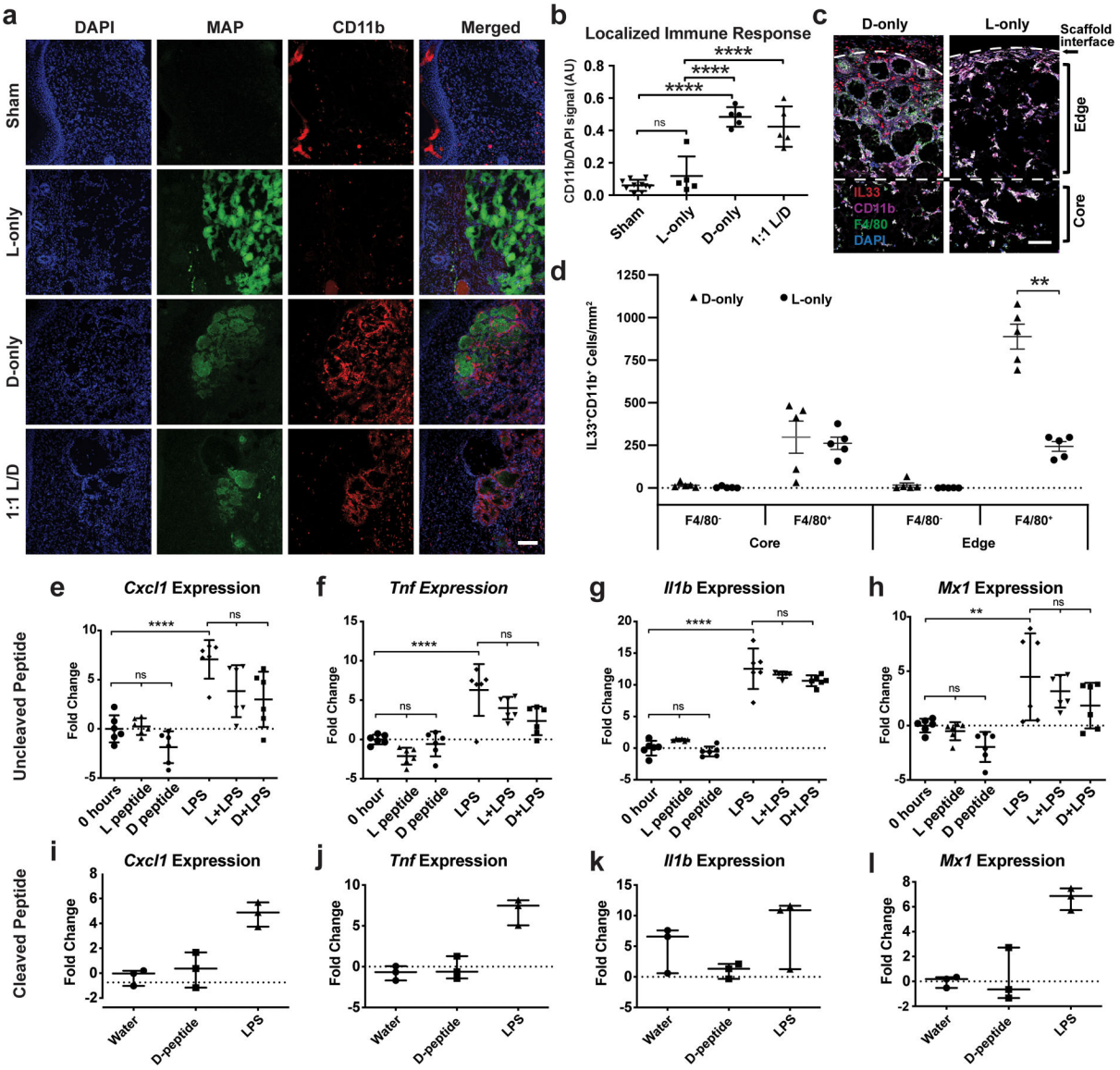

Figure 3. Peptide recognition by pattern recognition receptors is not required for myeloid cell recruitment.

a) Representative confocal immunofluorescent images staining myeloid cells ($CD11b^+$) within healed wounds of B6 mice in the absence or presence of the indicated hydrogel. Scale = 100μm**. b)** Quantification of $CD11b^+$ cellular infiltrate in healed tissue 21 days after wounding in the presence or absence of hydrogel. Each point represents average of 3 slides for each wound. All analysis is by one-way ANOVA (F-value (3,21): 41.10; **** denotes $p<0.0001$). **c-d**) Representative high-resolution confocal immunofluorescence imaging for CD11b, F4/80, DAPI, and IL-33 from subcutaneous implants of L- or D-MAP hydrogel implants (c) and quantification of IL-33 producing macrophages and other myeloid cells at hydrogel edge and core. n=5 B6 mice, mean +/− SEM (d), multiple t-tests adjusted for multiple comparisons using Holm-Sidak method (** denotes p=0.00014). Scale = 100μm. **e-h**) Murine bone marrow derived macrophages (BMDMs) from B6 mice were stimulated with 500 μg/ml of full-length L- or D- crosslinker peptide in the presence or absence of

lipopolysaccharide (10ng/ml) for 6 hours. Shown are qPCR results of 4 inflammatory genes from two separate experiment performed with n = 6. All analysis is by one-way ANOVA (Respective F-values (5, 30): 15.66, 17.62, 107.1, and 8.229, ** denotes p=0.009 and **** denotes p<0.0001) **i-l**) BMDMs were stimulated with LPS (10ng/ml) or cleaved D-crosslinker peptide (500μg/ml) that possessed an N-terminal D-amino acid. Experiment was performed in triplicate. All analysis is by one-way ANOVA (Respective F-values (2,6): 20.28, 30.86, 2.178, and 22.72). Data is plotted as a scatter plot showing the mean and standard deviation.

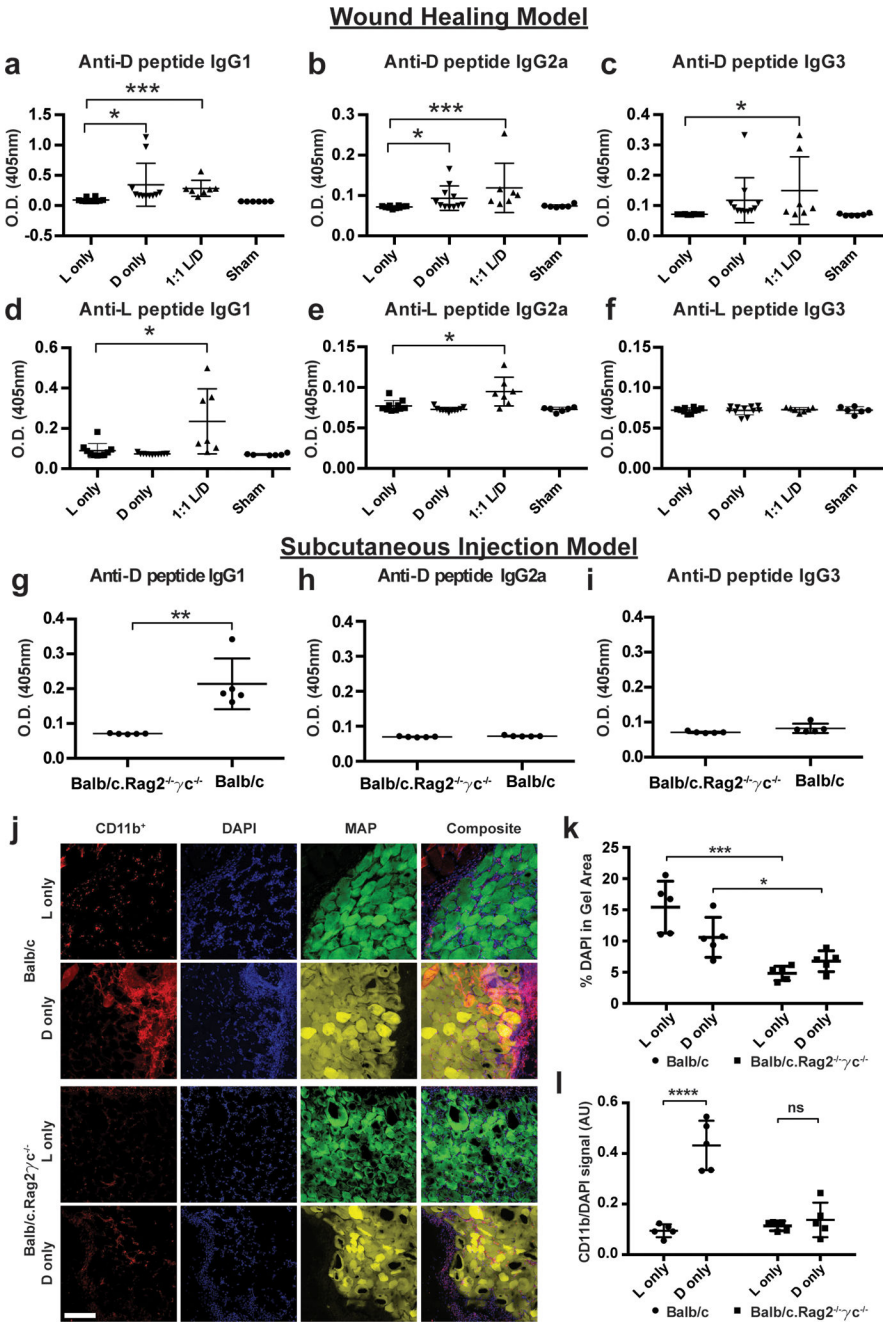

Figure 4. D-MAP induces antibody responses and recruitment of myeloid cells via adaptive immunity.

a-c) Measurement of anti-D specific IgG subtype antibodies by ELISA 21 days following wound healing experiments in SKH1 mice treated with indicated hydrogels. **d-f**) Measurement of anti-L specific IgG subtype antibodies by ELISA 21 days following wound healing experiments in SKH1 mice treated with indicated hydrogels. Each data point represents one animal and all analysis in a-f is by unpaired two-tailed t-test comparing each condition to L only. **g-i**) Measurement of anti-D specific IgG subtype antibodies in Balb/c or Balb/c.Rag2$^{-/-}\gamma c^{-/-}$ mice given a subcutaneous injection of D-MAP 21 days after injection.

Each data point represents one animal and all analysis in g-I is by unpaired two-tailed t-test (** denotes p=0.0022). **j-l**) Representative examples of confocal immunofluorescent imaging for CD11b, DAPI, and hydrogel from subcutaneous implants of L- or D-MAP hydrogel implants in Balb/c or Balb/c.Rag2$^{-/-}\gamma c^{-/-}$ mice. Scale = 200μm. (j) and quantification of total DAPI^{+} cells (k) and CD11b^{+} myeloid cells (l). Data is plotted as a scatter plot showing the mean and standard deviation. Each point represents average of 3 slides for each wound. All analysis is by unpaired two-tailed t-test (* denotes p=0.0455, *** denotes p=0.0006, **** denotes p<0.0001) represent statistical significance by student t-test for the comparison indicated.

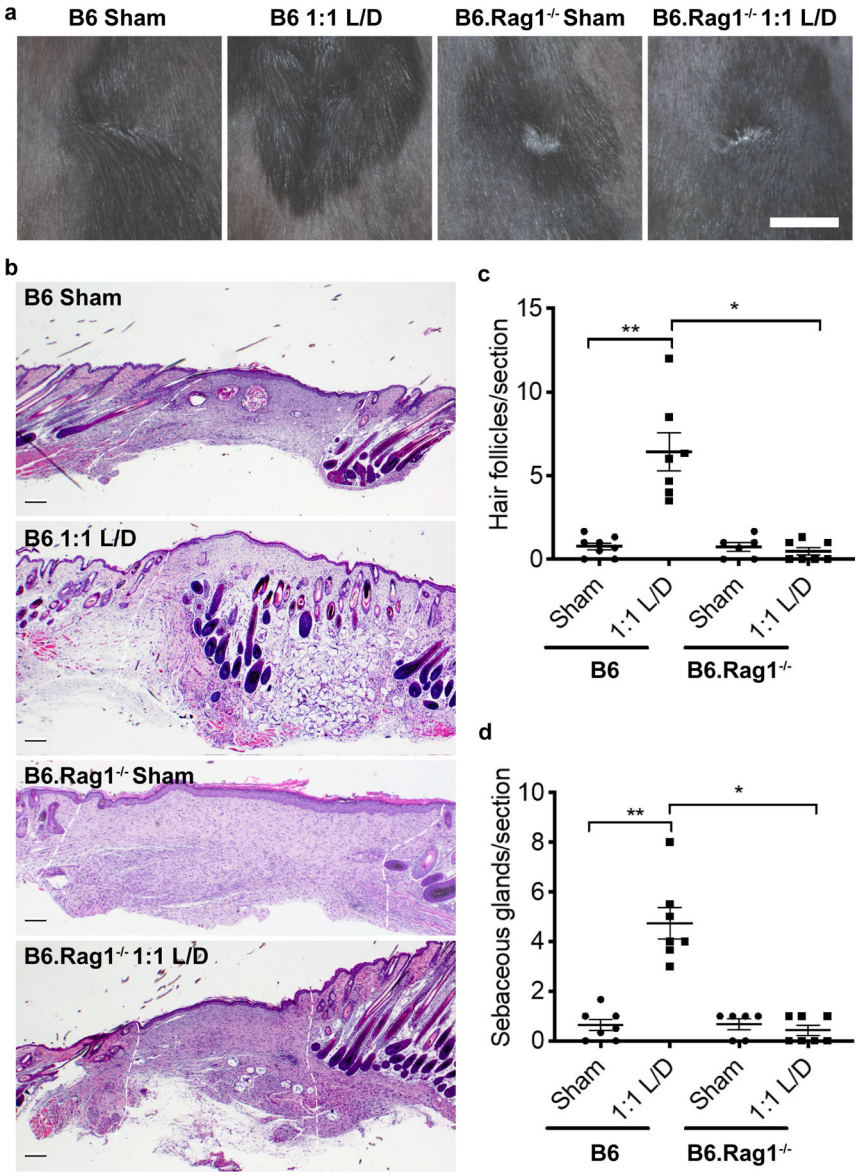

Figure 5. D-MAP requires an intact adaptive immunity to induce hair follicle neogenesis.

a) Representative examples of gross clinical images of healed splinted excisional wounds in B6 or B6.Rag1$^{-/-}$ mice by DSLR camera 17 days later treated as sham (no hydrogel) or 1:1 L/D-MAP treatment. Scale = 5mm. **b**) Histologic sections of healed tissue from B6 or B6.Rag1$^{-/-}$ mice. Scale = 200μm. White dashed lines denotes wounded area. Quantification of the average numbers of **c**) hair follicles and **d**) sebaceous glands from 3 histological sections per sample from B6 mice and B6.Rag1$^{-/-}$ mice. Data is plotted as a scatter plot showing the mean and SEM. * denotes two-tailed p=0.002 by Mann Whitney test, for inter-strain/identical treatment comparison and ** denotes p=0.0039 by Wilcoxon test for intra-strain/different treatment comparison.

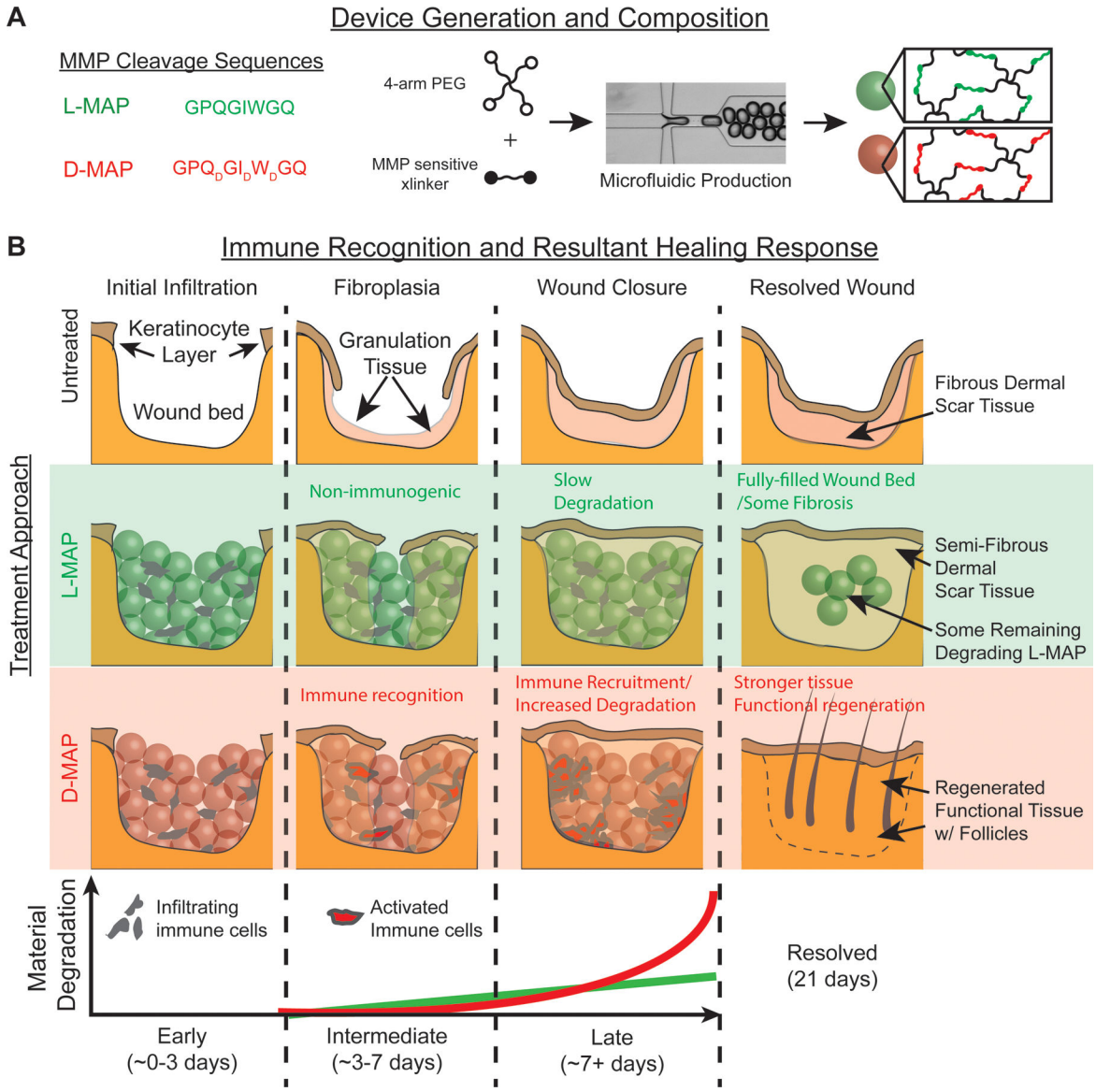

Figure 6. D-MAP changes the wound fate from scar formation to regeneration by type 2 immune activation.

a) Representation of amino acid chirality within the cross-linking peptides, microfluidic formation of the hydrogel microbeads incorporating L- or D- chirality peptides. **b)** The use of L- or D-MAP in a wound healing model demonstrates that both L- or D-MAP hydrogel fill the wound defect. While wounds that heal in the absence of hydrogel heal with an atrophic scar with loss of tissue, the epidermis forms over the scaffold in both cases and allows for increased dermal thickness. However, in the case of D-MAP, the hydrogel activates the adaptive immune system over time, resulting in tissue remodeling and skin regeneration as the adaptive immune system degrades the D-MAP scaffold.